

Control System Development and Flight Test Experience with the MQ-8B Fire Scout Vertical Take-Off Unmanned Aerial Vehicle (VTUAV)

James Downs Ron Prentice Scott Dalzell Adam Besachio
james.downs@ngc.com ron.prentice@ngc.com scott.dalzell@ngc.com adam.besachio@ngc.com
GNC Engineer GNC Engineer GNC Engineer GNC Engineer

Integrated Systems, Unmanned Systems
Northrop Grumman Corporation, Rancho Bernardo, CA

Christina M. Ivler Mark B. Tischler Mohammadreza Hossein Mansur
Civler@mail.arc.nasa.gov MTischler@mail.arc.nasa.gov HMansur@mail.arc.nasa.gov
Research Engineer, San Jose Senior Scientist Aerospace Engineer
State University Foundation Flight Control Group Leader

Aeroflightdynamics Directorate (AMRDEC)
U.S. Army Research, Development, and Engineering Command, Moffett Field, CA

Abstract

This paper describes the control system development of the MQ-8B Fire Scout autonomous helicopter. It includes a discussion of the system identification process and some details on implementing the identification output into a six degree of freedom simulation. Inner loop control law synthesis using classical, and two different modern design tools for meeting specific stability and performance metrics is also presented. This is followed by the details of the classical outer loop design process. Finally, some preliminary flight test results are presented from the successful initial flights.

NOMENCLATURE

Acronyms:

AFDD: U.S. Army Aeroflightdynamics Directorate
CIFER[®]: Comprehensive Identification from Frequency Responses
CONDUIT[®]: Control Designer's Unified Interface
CRDA: Cooperative Research and Development Agreement
DARPA: Defense Advanced Research Projects Agency
EMD: Engineering Manufacturing Design
GNC: Guidance Navigation and Control
GPS: Global Positioning System
INS: Inertial Navigation System
MIMO: Multi-Input/Multi-Output
NGC: Northrop-Grumman Corporation

Presented at the American Helicopter Society 63rd Annual Forum, Virginia Beach, VA, May 1-3, 2007.
Copyright © 2007 by the American Helicopter Society International, Inc. All rights reserved.

OGE: Out of ground effect
P5: Prototype 5
UAV: Unmanned Air Vehicle
VTUAV: Vertical Take-off Unmanned Air Vehicle

Symbols

M State derivative matrix
F State matrix
G Control matrix
H Output state matrix

L Derivative for specific rolling moment
M Derivative for specific pitching moment
N Derivative for specific yawing moment
p Fuselage roll rate
q Fuselage pitch rate
r Fuselage yaw rate
u Control vector
u Longitudinal velocity
v Lateral velocity
w Vertical velocity
X Derivative for specific longitudinal force
x State vector

Y	Derivative for specific lateral force
\mathbf{y}	Output vector
Z	Derivative for specific vertical force
δ_{lat}	Lateral cyclic input
δ_{lon}	Longitudinal cyclic input
δ_{ped}	Pedal input
δ_{col}	Collective input
φ	Fuselage roll angle
θ	Fuselage pitch angle
δ_{MRRA}	Main Rotor Right Aft input
δ_{MRL}	Main Rotor Left input
δ_{MRRF}	Main Rotor Right Forward input

Introduction

The RQ-8A (Figure 1) was developed in 2000 as a response to a Navy RFP for a ship-based VTOL unmanned air vehicle. An Engineering, Manufacturing and Design (EMD) contract was awarded in February 2000. Since then, the RQ-8A has accumulated some 200 hours of flight time and in January of 2006, successfully performed an autonomous landing on the USS Nashville near Patuxent River NAS.

The MQ-8B (Figure 2) is an outgrowth of the RQ-8A to include an upgraded transmission allowing greater power, a four blade rotor system, the addition of sponsons and minor modifications to the airframe. In addition the actuation system was modified by

removing the mechanical mixer and moving the cyclic actuators to just below the swashplate. The mixer function, which mapped cyclic motion to swashplate motion is now accomplished in software along with an aerodynamic de-coupling mixer.

The MQ-8B is currently in engineering development, undergoing flight testing at the Navy's Patuxent River facility. Eventually the Fire Scout will be a key component of the Navy's new Littoral Combat Ship (LCS), fulfilling the functions of tactical reconnaissance, target designation, mine detection and weapons delivery amongst a host of other capabilities.

The following sections discuss the GNC development of the MQ-8B. This included system identification from flight data (model ID) using a manned version of the MQ-8B. The stability and control derivatives and trim data from this process were used to update the RQ-8A 6 degree-of-freedom nonlinear simulation. The identified model was also used to develop a separate SIMULINK based linear simulation. Once the basic dynamics of the air vehicle were established, the control law gains for the inner Autopilot loops were synthesized using a combination of classical and modern methods. Outer loop control law gains were then developed by classical methods.



Figure 1. RQ-8A.



Figure 2. MQ-8B first hover

System Identification using CIPHER[®]

A database of accurate state space models across the flight envelope was needed for control law development of MQ-8B. Rotorcraft system identification is difficult by nature as an accurate model requires at least six degree-of-freedom, the rotor produces large vibrations, and the vehicle is often dynamically unstable (Ref. 1). Frequency domain methods are well suited to the rotorcraft problem, for many reasons including:

1. Frequency domain analysis eliminates the bias effect of noise in the measured responses. Uncorrelated process noise also drops out of the frequency-response identification.
2. The analysis produces a coherence function which is an independent measure of signal quality and linearity of a frequency response.
3. The process allows model fitting only over frequency ranges that are accurate.
4. Time delays can be identified directly.
5. The process has the ability to identify dynamically unstable aircraft.

The software CIPHER[®], Comprehensive Identification from FrEquency Responses, was developed by the Army/NASA Rotorcraft division at Ames Research Center as an integrated environment for converting flight data to frequency responses, identifying state-space models, calculating handling-qualities,

implementing frequency response arithmetic, and performing many other useful functions. The CIPHER[®] software was chosen for use in MQ-8B bare airframe system identification for the reasons listed above and because the software had been used with satisfactory results in the RQ-8A program (Ref. 2).

System Identification using CIPHER[®] consists of the following steps, which are discussed in greater detail in References 1 and 3.

1. Frequency response identification from flight data (Chirp-Z transform)
 - Multi-input conditioning is used to eliminate the influence of off-axis inputs. A composite windowing technique is used to improve the frequency range of accuracy by combining a weighted average of multiple windows.
2. State space model identification
 - Model parameters are optimized to provide the best match to frequency responses identified from flight data. A coherence weighted cost function (J) is used to quantify the match between flight data and the state-space model. Then the theoretical accuracy parameters, Insensitivity (I) and Cramer-Rao Bound (CR), are used to evaluate the uniqueness of each parameter. Insensitivity is measure of the insensitivity of the cost function to a percent change in the identified parameter. The Cramer Rao Bound is the estimated minimum

standard deviation of a parameter that would be calculated after many repeated trials.

3. Time domain verification

The state-space model is driven with flight data (not used in the identification), and the outputs of the model are evaluated against the real flight data. Doublets in each axis are usually used for verification.

The following sections of this paper discuss the results of each of these steps in detail for the MQ-8B.

Flight Testing with Manned Approximation of MQ-8B

System identification is generally performed at various speeds across the flight envelope. For the MQ-8B, a state-space model is identified at each speed that is to be gain scheduled in the control laws. The models are stitched together to create a nonlinear simulation. This method is discussed in detail in Reference 4.

The flight maneuver that is used for the identification of frequency responses is the frequency sweep. This is a maneuver that can either be performed by a pilot or automated. In this case, the frequency sweeps were performed by a pilot in a manned version of the MQ-8B. The maneuver starts with a low frequency sinusoidal shaped input and increases in frequency as time progresses. The maneuver is typically 80-120 seconds long. Figure 3 gives an example of a piloted frequency sweep input and response. This maneuver provides excellent spectral content for the purpose of system identification.

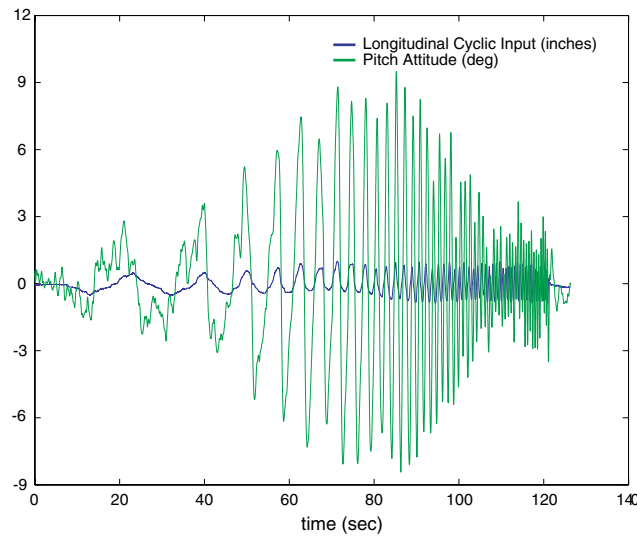


Figure 3. Frequency sweep.

The frequency sweeps were performed in each axis (pitch, roll, yaw, vertical), for the flight conditions shown in Table 1. Verification doublets are also

collected at each of these flight conditions to be used for time domain checks of the final models.

Table 1. Flight test matrix for system identification.

Flight Condition	Weight	C.G.	Altitude
OGE hover	2900 lbs	Mid	OGE (100 ft)
40 kts	2900 lbs	Mid	5,000 ft
70 kts	2900 lbs	Mid	5,000 ft
100 kts	2900 lbs	Mid	5,000 ft

Frequency-Response Identification

The frequency-responses for the MQ-8B are identified (with CIPHER[®]) from the frequency-sweep data. The input signals include δ_{lon} , δ_{lat} , δ_{ped} , and δ_{col} . The output signals are p , q , r , a_x , a_y , a_z , \dot{u} , \dot{v} , \dot{w} , α , β . The velocity derivative signals \dot{u} , \dot{v} , and \dot{w} were reconstructed using the kinematic relationships shown in the following equations.

$$\dot{u} = a_x - g\theta - qw_0 + rv_0 \quad (1)$$

$$\dot{v} = a_y + g\phi - ru_0 + pw_0 \quad (2)$$

$$\dot{w} = a_z - pv_0 + qu_0 \quad (3)$$

These reconstructed velocity derivatives were used in the identification rather than the velocity signals generated from the Embedded GPS/INS, which were seen to exhibit poor coherence.

Although the identified frequency-responses are not shown in this section of the paper, some examples are shown by Figure 4 and Figure 5 of the next section. These figures show the high quality of the frequency responses as indicated by their smooth shape and good coherence.

Identified State-Space Model

The model structure for the state-space identification was chosen based on the frequency responses that were determined from flight data. The level of coupling was determined by examining the coherence of the off-axes responses. High coherence indicates a coupled response, whereas a low coherence indicates that the output in question was not excited by the control input. For example, the coherence between pitch rate (q) and lateral stick input (δ_{lat}) is nearly zero. This indicates that lateral stick input does not excite the pitch response. Therefore, stability and control derivatives that are

related to the dynamic response between lateral inputs or lateral responses to pitch-rate should be eliminated. Therefore, $M_{\delta_{lat}}$, M_p , and M_v are set to zero before optimizing the state-space model (Ref. 1). This approach was used on all frequency-responses with very low coherence to eliminate the corresponding off-axis derivatives before optimization began.

Rotor inflow dynamics are not part of the quasi-steady mode structure, which thereby restricts the frequency range of accuracy for the vertical acceleration to collective (a_z/δ_{col}) to the region near cross-over (0.2-2 rad/sec), where these dynamics are less significant.

The engine dynamics have a large influence on the p/δ_{col} , q/δ_{col} , r/δ_{col} responses for MQ-8B at all flight conditions. To model these dynamics, engine states were included in the model. The rotor response with respect to the fixed frame (Ω) was modeled as the following second-order system, as done by Harding for the AH-64D (Ref. 5).

$$\frac{\Omega}{\delta_{col}} = \frac{K_{\delta_{col}}}{s^2 + 2\zeta\omega s + \omega^2} \quad (4)$$

A Taylor series expansion approximation is used for torque ($\dot{\eta}_T = T$ where T is engine torque):

$$\dot{\eta}_T = T_{\dot{\Omega}}\dot{\Omega} + T_{\Omega}\Omega + T_r r + T_w w + T_{\delta_{ped}}\delta_{ped} \quad (5)$$

The structure of the quasi-steady model is shown below:

$$M\dot{x} = Fx + Gu \quad (6)$$

$$x = [u \ v \ w \ p \ q \ r \ \phi \ \theta \ \Omega_R \ \Omega \ \dot{\Omega} \ \eta_T]^T \quad (7)$$

Note that $\Omega = \Omega_R - r$, where Ω_R is the rotor response with respect to the fuselage (Ω is defined in the opposite sign of fuselage yaw rate, r).

Speed Derivatives

The identification of the speed damping derivatives (X_u, Y_v) and speed stability derivatives (M_u, L_v, N_v) is often problematic for hovering flight because these derivatives are important only at low frequency where frequency-response accuracy is generally low. As discussed in Reference 1, these derivatives can be accurately isolated as demonstrated in this section. The

longitudinal speed-damping derivative (X_u) can be approximated by Eq. (8), which is valid at low frequency.

$$\dot{u} = X_u u - g\theta \quad (8)$$

Then by performing a Laplace transform the equation becomes:

$$\frac{\dot{u}}{q} = \frac{-g}{s - X_u} \quad (9)$$

A similar relationship can be used to constrain Y_v in the overall identification by using the frequency response \dot{v}/p . The speed-stability derivatives can be calculated with the trim data using Eqs. (10)-(12) (Ref. 1).

$$M_u = -M_{\delta_{lon}} \left(\frac{\Delta\delta_{lon}}{\Delta u} \right) + M_w \left(\frac{Z_u}{Z_w} \right) \quad (10)$$

$$L_v = - \left[L_{\delta_{lat}} \left(\frac{\Delta\delta_{lat}}{\Delta v} \right) + L_{\delta_{ped}} \left(\frac{\Delta\delta_{ped}}{\Delta v} \right) \right] \quad (11)$$

$$N_v = -N_{\delta_{ped}} \left(\frac{\Delta\delta_{ped}}{\Delta v} \right) \quad (12)$$

The needed control gradients can be calculated from a series of trim points. For the MQ-8B identification, the trim constraint for N_v was implemented within the model setup because low frequency information for the yaw rate response was poor, causing the N_v derivative to become insensitive. This constraint allowed for proper identification of the N_v derivative even without low frequency information. Although the constraints were not needed for M_u and L_v , they were used to check the magnitude and sign of the identified derivatives.

Identified Model

As an example of the accurate predictive capability of the identified models, some results will be shown from the hover flight condition. The models for the other flight conditions given in Table 1 proved to be of comparable accuracy, but are not shown in this paper.

The cost functions for the identified hover model, as given in Table 2, are an indication of how well the identified model matches the frequency responses from flight data. An average cost of less than 100 is considered acceptable. The individual cost functions should be less than 150-200. As seen in Table 2, the only

costs outside of the guidelines correspond to the off-axis responses p/δ_{lon} and a_y/δ_{lon} . However, most individual costs are well below the guideline and the average cost is below 100, indicating that the model is still a very good match to the flight data.

Table 2. Costs for identified model at hover.

Transfer Function	Model Cost
a_y/δ_{lat}	57.582
\dot{v}/δ_{lat}	59.455
p/δ_{lat}	32.095
a_x/δ_{lon}	112.005
a_y/δ_{lon}	242.670
\dot{u}/δ_{lon}	45.934
p/δ_{lon}	214.320
q/δ_{lon}	60.217
a_x/δ_{col}	98.871
a_z/δ_{col}	30.889
\dot{u}/δ_{col}	109.231
p/δ_{col}	123.783
r/δ_{col}	80.624
Ω/δ_{col}	64.940
T/δ_{col}	119.571
p/δ_{ped}	16.451
q/δ_{ped}	10.670
r/δ_{ped}	89.758
T/δ_{ped}	36.386
v/ϕ	46.749
Average	79.427

Comparisons of the identified model fit to the flight data are shown for the on-axis longitudinal and heave responses in Figure 4 and Figure 5. These figures indicate that the model and the flight data are in good

agreement. The overlays of the model to flight data for all other frequency responses are not shown in this paper for brevity. In general, the model accuracy is proven to be acceptable by the cost functions in Table 2.

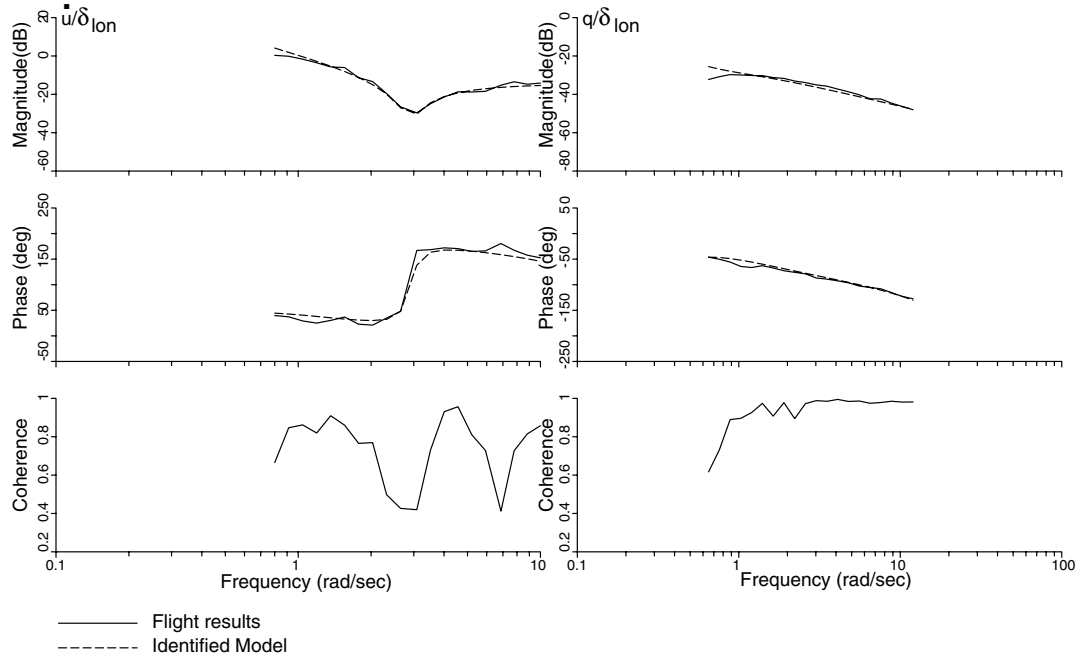


Figure 4. Comparison of flight data and model (longitudinal responses).

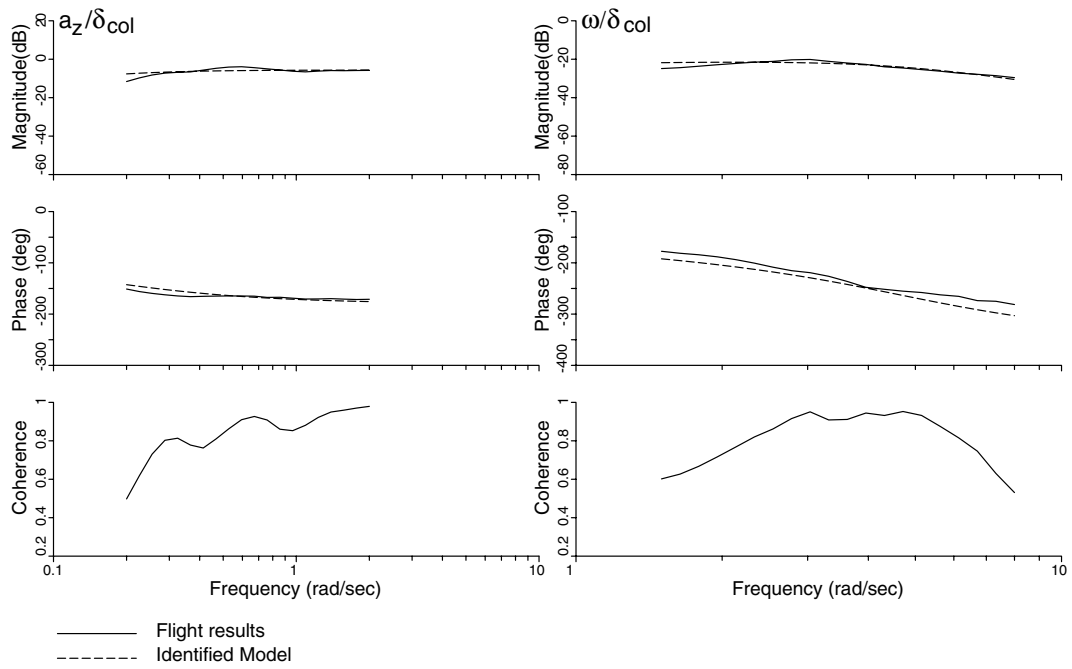


Figure 5. Comparison of flight data and model (heave responses).

Time Domain Verification

The identified model is verified in the time domain to ensure that it can accurately predict the aircraft dynamic response. The pilot's inputs from flight doublets are used to excite the model, and the model responses and the aircraft responses to this doublet are then compared. If the responses match, then the model has good predictive accuracy.

The longitudinal verification results for hover are given in Figure 6. Only the dominant responses to the longitudinal doublet are shown. As seen in the figure, the model matches the flight data well in the time domain. The mismatch in the yaw rate response r reflects an error in the long term response, likely a result of poor frequency response coherence at low frequency, but the short term agreement is satisfactory.

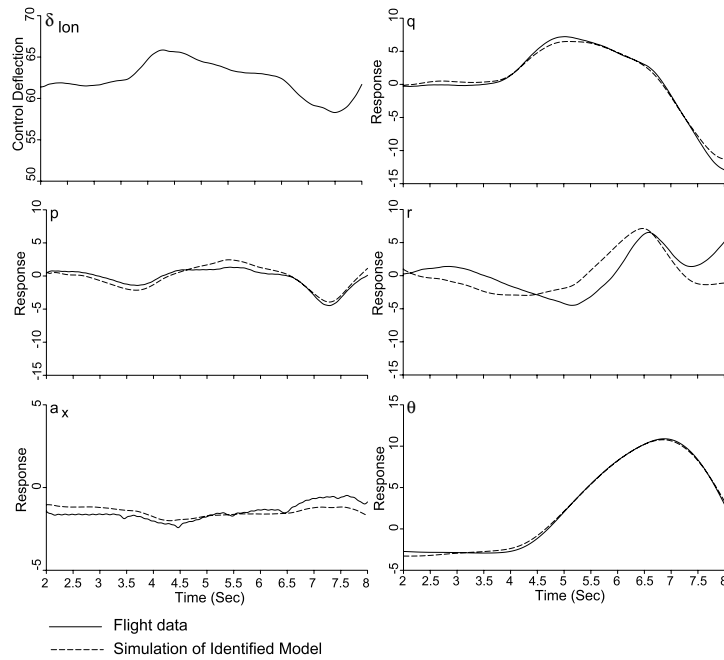


Figure 6. Longitudinal verification results.

Figure 7 indicates that the model matches the flight data well in the time domain for collective responses. The model has excellent predictive accuracy for vertical acceleration and torque, indicating that the engine model is accurate. However, similar to the longitudinal case there is some error in the yaw rate response. The lateral and directional maneuvers show similar predictive accuracy to those presented here, but are not shown in this paper.

Overall, the model matches the flight data well in the time-domain for all control inputs. All the time-domain cost functions were within the acceptable range of 1-2, which indicates good predictive capability (Ref. 1). The agreement of torque and rotor speed is excellent for all control inputs. Similar results were seen in the forward flight cases.

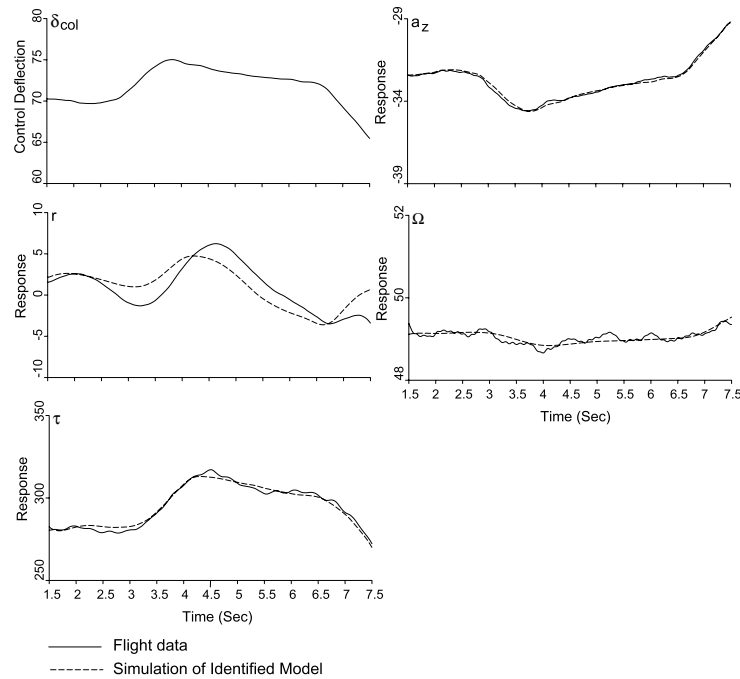


Figure 7. Collective verification results.

Building a Full-Flight Envelope Simulation

System identification produces individual state-space perturbation models that are accurate at each of discrete (reference) flight condition for which frequency-sweep flight testing is conducted. These models are highly useful for control law design and analysis to produce a gain schedule over the flight envelope. “Model stitching” refers to the process of combining these discrete state-space perturbation models and the associated trim flight-test data into a single continuous full-envelope flight-dynamics simulation model.

The predominant variables that effect the helicopter dynamic response are trim airspeed (V_0), density (ρ_0) and aircraft configuration (e.g., external stores or clean). State-space models are identified for each reference flight condition, and are stored in table look-up form. Flight test data also provide associated trim control locations and trim state vector (x_o, u_o) at each reference flight condition. Then, the appropriate values of the stability and control derivatives (A, B, C, D matrices) can then be interpolated for an instantaneous flight speed, air density, and aircraft configuration. Further the perturbation states and controls are determined based on difference between the total instantaneous and trim values to produce the instantaneous accelerations. This forms the basis of a continuous full-flight envelope “stitched model” which is useful for evaluation of control system initialization and mode transition transients, hardware-in-the-loop testing, and especially for use in a full-envelope pilot training simulator. An

example of this technique is presented in Reference 4 for the B206 helicopter and is quite similar to the approach used for the Fire Scout.

Control System Development and Overview

A SIMULINK block diagram of the control system architecture is shown in Figure 8. The left-most blocks represent the outer-loop navigation controllers. From the top down they consist of the following:

1. Separate downtrack controllers for land-based and ship-based operations.
2. A velocity controller (both airspeed and groundspeed)
3. A ship-based crosstrack controller
4. A course controller
5. A land-based crosstrack controller.
6. A ship-based altitude controller
7. A land-based altitude controller.

Most of these controllers are simple PID type feedback loops, although for ship-based operation lateral and longitudinal accelerations are utilized.

These navigation (outer loop) modes provide pitch, roll, yaw and vertical speed commands to the four Autopilot PID controllers. The Autopilot in turn outputs commands to a mixer which has two functions; it maps the pedal and virtual cyclic commands to equivalent commands to the pedal and the three swashplate actuators, and it decouples the controller induced motion.

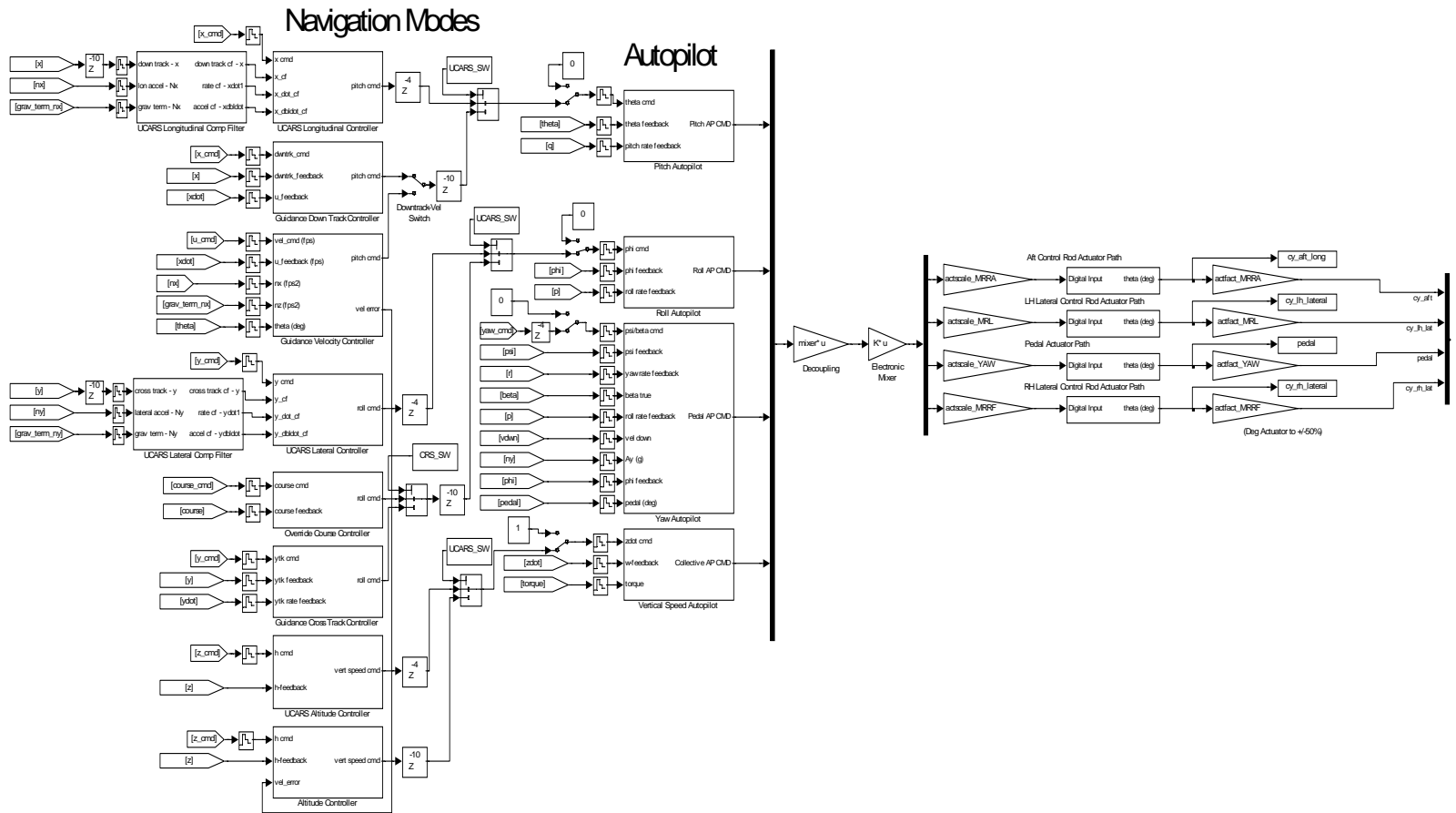


Figure 8. Control law architecture for MQ-8B.

The Autopilot gains were developed using a Northrop-Grumman developed “Genetic Algorithm” the details of which are discussed in the following sections. The set of gains generated from this algorithm were considered baseline which were often refined using classical methods involving root loci and frequency responses. The gains for the outer navigation loops were obtained from strictly classical methods. As a confidence building measure for the critical hover flight condition, a parallel Autopilot gain synthesis was conducted by the U.S. Army AFDD using their CONDUIT® tool (Ref. 6). The stability and performance results of each design methodology were compared and there were no major differences between the two and the Northrop Grumman gain set was used for the first flight tests.

CONDUIT Based Control Law Design

This section of the paper discusses the optimization of the Fire Scout MQ-8B control system ACAH (attitude command/attitude hold) gains for the hover flight condition (2900 lbs) using the CONDUIT® tool. CONDUIT® is a software package that provides an environment for aircraft flight control design, optimization, and evaluation (Ref. 6). CONDUIT® was applied to optimization of the ACAH pitch, roll, yaw and heave control loops. The goal of the optimization was to achieve comparable performance as the RQ-8A version of Fire Scout (Ref. 2).

The CONDUIT® analysis of the control system was based on a linear SIMULINK® block diagram of the control laws for MQ-8B. The vehicle model embedded in the SIMULINK® block diagram was identified from frequency sweep flight tests using CIPHER® as discussed earlier.

The stability and performance specifications used to drive the optimization of the control laws were carefully

selected for applicability to unmanned rotorcraft operations. Some specifications were chosen from the ADS-33 rotorcraft handling qualities requirements document (Ref. 7) because they also provide desirable flying qualities for a full-scale UAV. The required gain and phase margins are based on the military specification for flight control systems, MIL-F-9490D (Ref. 8). Most of those specifications were repeated from the successful experience with the prior Fire Scout configuration, RQ-8A (Ref. 2). These requirements ensured that the vehicle would be capable of precision maneuvering and ship board landing operations. The addition of coupling and disturbance rejection bandwidth specifications was based on recent AFDD experience from other helicopter programs, such as the AH-64D (Ref. 9).

The design specifications were grouped into the three categories that define how the optimization prioritizes each requirement. The categories are known as Hard Constraints, Soft Constraints, and Summed Objectives. Hard constraints are considered in the first phase of the optimization. The set of Hard Constraints included requirements crucial to the stability of the aircraft (eigenvalues in left-half plane and stability margins). During the second phase of the optimization soft constraints, which include handling qualities and performance criteria, must be satisfied while ensuring that the Hard Constraints remain satisfied. The last phase of the optimization begins once all of the Hard and Soft Constraints are met. The optimization minimizes a set of Summed Objectives during this phase while ensuring that all other specifications continue to be met. Generally actuator RMS and cross-over frequency are chosen as summed objectives. The following table provides a complete description of the specifications that were selected for the MQ-8B control law optimization.

Table 3. Stability, handling qualities and performance specifications.

Specification	Description	Constraint Type	Axes
EigLcG1	Eigenvalues in L.H.P.	Hard	Pitch, Roll, Yaw, Heave
StbMgG1	Gain and Phase Margin (45 deg, 6 dB)	Hard	Pitch, Roll, Yaw, Heave
BnwPiH1	Pitch bandwidth for acquisition and tracking (ADS-33)	Soft	Pitch
BnwRoH2	Roll bandwidth for other M.T.E.'s (ADS-33)	Soft	Roll
BnwYaH1	Yaw bandwidth for acquisition and tracking (ADS-33)	Soft	Yaw
CouPRH2	Coupling between pitch and roll	Soft	Pitch/Roll
CouYaH2	Coupling between collective and yaw	Soft	Yaw

Specification	Description	Constraint Type	Axes
DstBwG1	Disturbance rejection bandwidth	Soft	Pitch, Roll, Yaw, Heave
FrqGnG1	Average frequency response (at low frequency to minimize steady-state error)	Soft	Pitch, Roll, Yaw, Heave
FrqHeH2	Heave response for ship board landing (ADS-33)	Soft	Heave
HldNmH1	Normalized attitude hold response to disturbances	Soft	Pitch, Roll, Yaw
OvsTimG1	Damping ratio	Soft	Pitch, Roll, Yaw, Heave
OvsTqG1	Torque response (torque damping)	Soft	Heave
CrsLnG1	Cross-over frequency	Summed Objective	Pitch, Roll, Yaw, Heave
RmsAcG1	Actuator RMS	Summed Objective	Pitch, Roll, Yaw, Heave

A family of optimized designs was developed with increasing levels of disturbance rejection bandwidth. Higher disturbance rejection bandwidth improves the hold functions in turbulent/noisy conditions at the cost of higher actuator activity, increased cross-over frequency and lower phase margin. A similar approach was implemented in the AH-64D Apache flight control law design (Ref. 9). Disturbance rejection bandwidth is

defined as the frequency at which the Bode magnitude plot of the sensitivity function (Eq. (13)) crosses the -3 dB line, for the system shown in Figure 9.

$$S(s) = \frac{y(s)}{\delta_g(s)} = \frac{I}{I + G(s)C(s)H(s)} \quad (13)$$

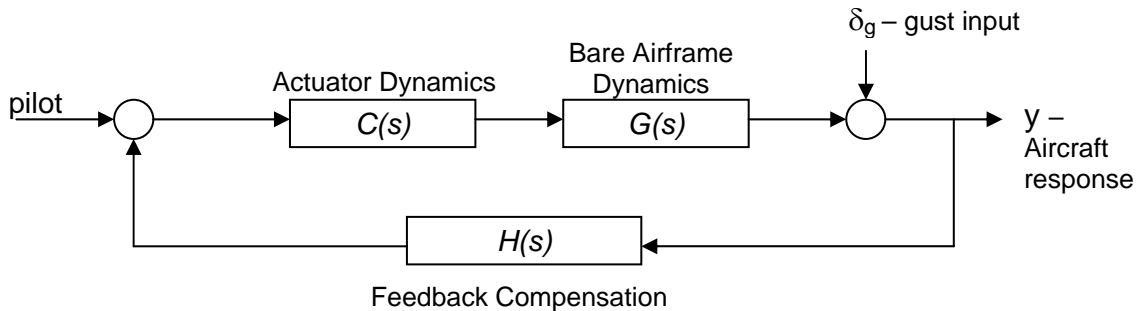


Figure 9. Block diagram for a typical aircraft.

The “Design Margin Optimization” batch mode utility in CONDUIT[®] was used to incrementally extend the acceptable boundary (Level 1) for the disturbance rejection specification, and then optimize at each point. The family of designs for the hover yaw autopilot is shown by Figure 10. This figure exemplifies the trade-offs between disturbance rejection, actuator activity and phase margin. Figure 10 indicates that increased

disturbance rejection bandwidth has the general effect of increasing the cross-over frequency and actuator activity, whereas the phase margin had a decreasing trend. Due to the influence of other specifications, such as bandwidth and damping, these trends are not monotonic. The results for the other control axes demonstrated comparable design tradeoffs.

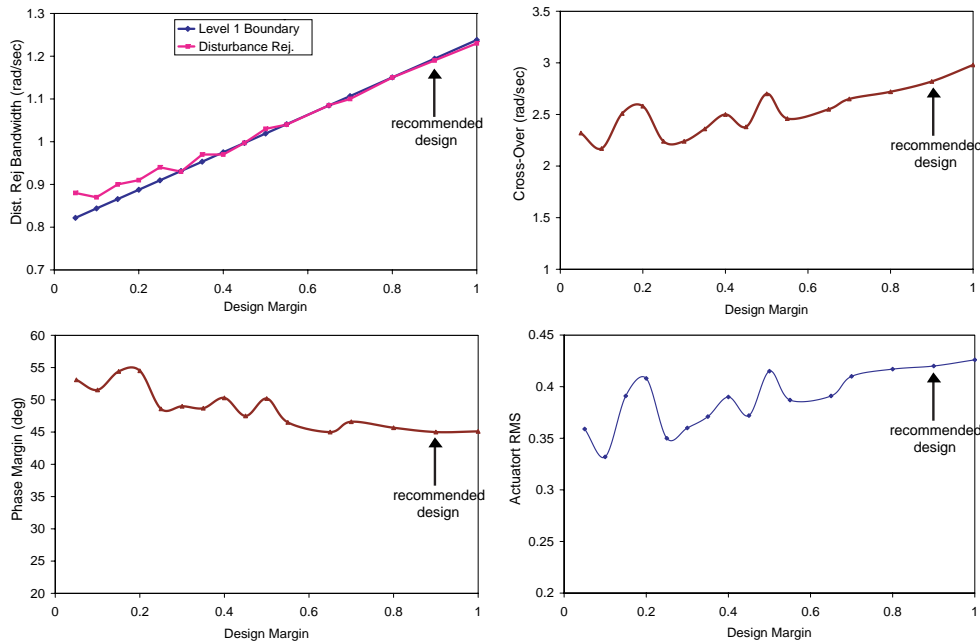


Figure 10. Family of designs for yaw autopilot (ACAH).

Results

One recommended design was chosen from the family of designs (Figure 10). The 90% design margin case (for disturbance rejection bandwidth) was the recommended design. This gain set was selected because it provides a good balance of nearly maximized disturbance rejection, reasonable cross-over frequency, and meets the Level 1 requirements for stability margin.

As mentioned previously, the goal of this optimization was to provide comparable stability and performance as compared to the RQ-8A. The following table compares the control system characteristics for the MQ-8B model at 2900 lbs with CONDUIT[®] control law gains and the RQ-8A model with its current control law gains at 2900 lbs.

Table 4. Comparison of RQ-8A and MQ-8B modeled performance.

	Pitch G.M. (dB)	Pitch P.M. (deg)	Roll G.M. (dB)	Roll P.M. (deg)	Yaw G.M. (dB)	Yaw P.M. (deg)	Collective G.M. (dB)	Collective P.M. (deg)
RQ-8A	9.72	41.83	6.26	26.2	12.9	79.75	19.9	86.9
MQ-8B	8.5	46.1	8.32	48.7	16.7	45	7.1	45

	Pitch Crossover (rad/s)	Roll Crossover (rad/s)	Yaw Crossover (rad/s)	Collective Crossover (rad/s)	Pitch D.R.B. (rad/s)	Roll D.R.B. (rad/s)	Yaw D.R.B. (rad/s)	Collective D.R.B. (rad/s)
RQ-8A	3.24	3.98	3.45	1.44	1.1	1.77	1.05	1.4
MQ-8B	3.92	4.18	2.82	2.14	0.96	1.4	1.1942	0.98

G.M. = gain margin, P.M. = phase margin, D.R.B. = disturbance rejection bandwidth

Table 4 indicates that this design approach produced a design for MQ-8B that meets the stability margin requirements in all axes. The design produced cross-over frequencies which were reasonable in comparison with RQ-8A. The disturbance rejection bandwidth improved in the MQ-8B design for the pitch and roll axes, and was comparable for yaw. Overall, the goal to provide comparable stability and performance as the RQ-8A was met by this design.

The CONDUIT[®] analysis window for the recommended design is given by Figure 11. This figure shows that the design meets the Level 1 requirements (desirable) for all specifications except yaw coupling and torque damping ratio. These two specifications were not optimized (check only) because the control system was not able to move these characteristics into Level 1 without severely restricting the design space (i.e., moving cross-over frequencies undesirably high for yaw and undesirably low for heave).

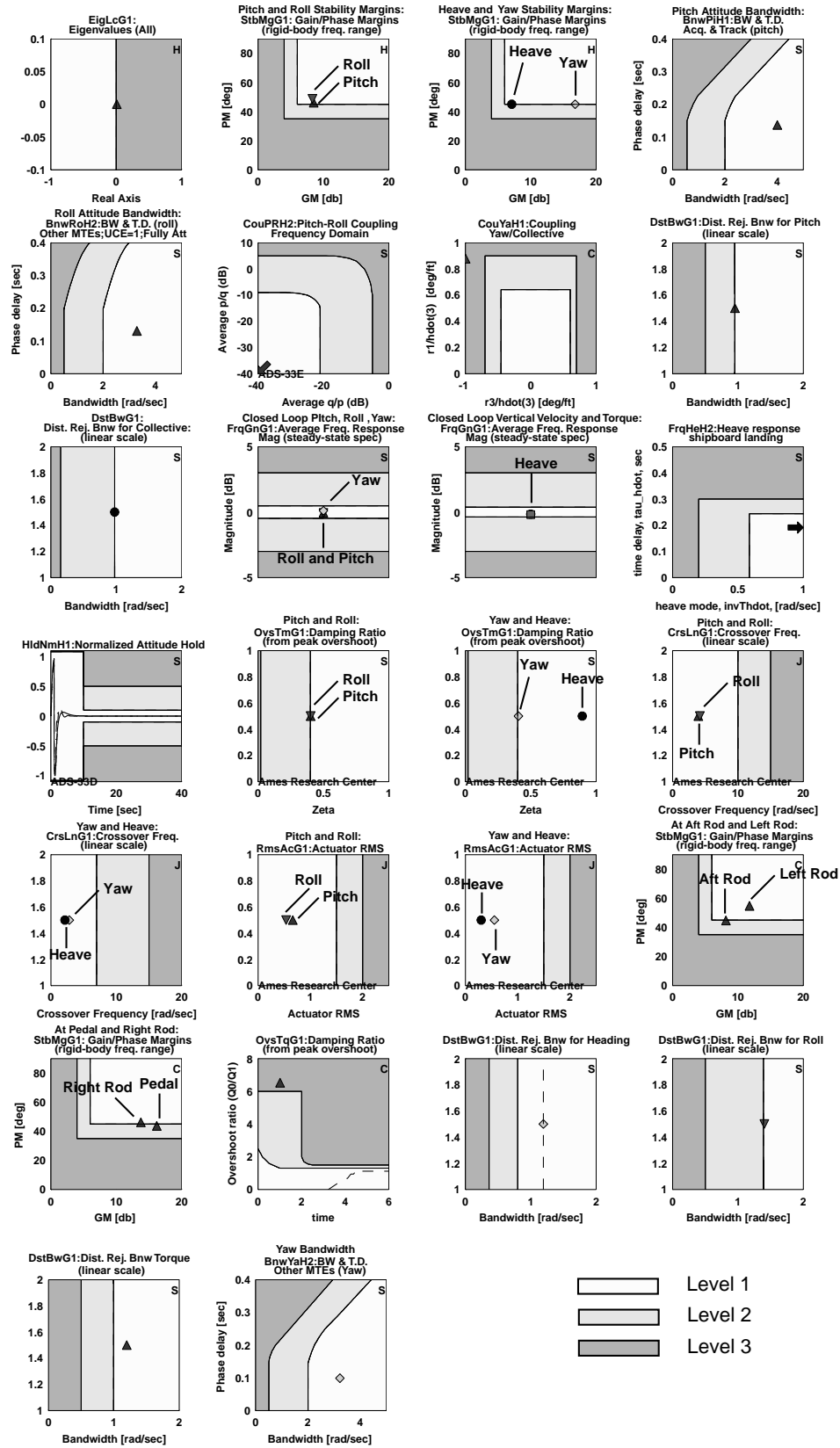


Figure 11. CONDUIT[®] analysis window for selected design.

The step responses for this design are shown in Figures 12-15. These figures indicate that responses are reasonable in the time domain and that they demonstrate acceptable damping, rise time, and settling time.

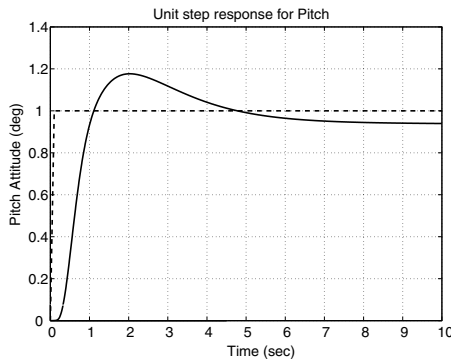


Figure 12. Pitch step.

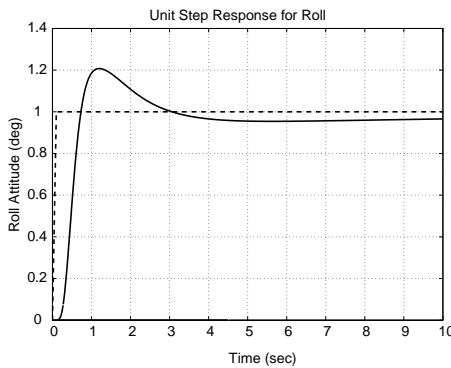


Figure 13. Roll step.

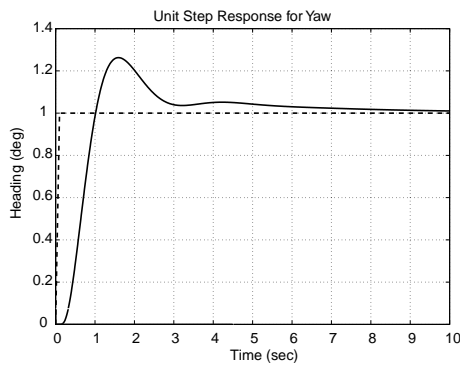


Figure 14. Yaw step.

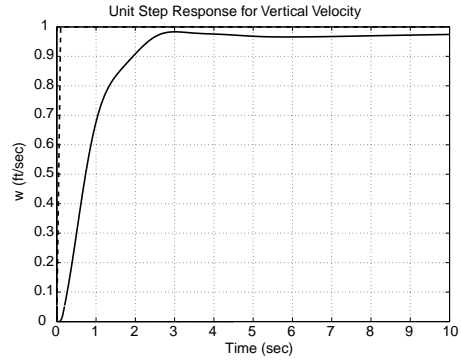


Figure 15. Heave step.

Robustness Analysis

A robustness analysis evaluates the sensitivity of the control system to uncertainties in the vehicle dynamics. This is of special consideration for a UAV because it relies completely on the control system to safely perform autonomous operations. Robustness is evaluated by randomly perturbing elements of the CIFER identified model and examining the effects on the control system performance. A robustness analysis was performed with CONDUIT[®] based on the theoretical accuracy metrics (Cramer-Rao bounds) provided by CIFER[®]. Cramer-Rao bounds are a measure of the expected minimum standard deviation of an identified stability or control derivative (Ref. 1), thus it makes sense to measure robustness in terms of perturbations in proportion to them. CONDUIT[®] has the capability to import a state-space model from CIFER[®] and perturb the stability derivatives based on the Cramer-Rao percents from the CIFER[®] identification.

Figure 16 shows the eigenvalues and stability margins for 100 random perturbations at 3σ , three times the expected standard deviation of each derivative. The stability margins vary with the perturbations, most noticeably in the heave response, but the system remains stable.

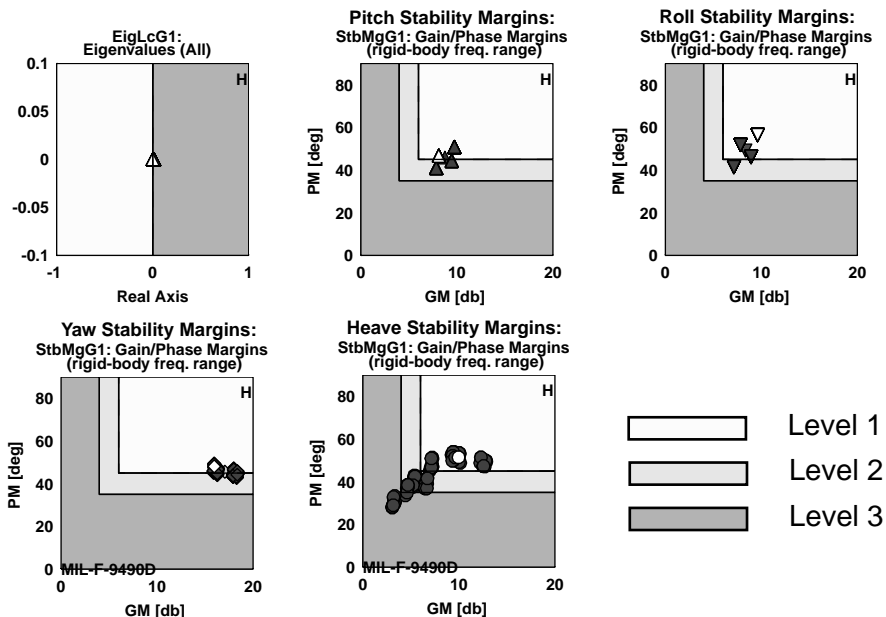


Figure 16. Stability results for 100 random perturbations at 3σ .

Genetic Algorithm Based Autopilot Design

As a compliment to the above CONDUIT[®] based design, the Fire Scout GNC team developed a genetic algorithm to simultaneously satisfy a set of classical design criteria in both the time and frequency domains across all control axes, i.e. roll, pitch, yaw, and vertical. The genetic algorithm approach blankets the solution space with a random distribution of initial gains, which are then “evolved” through an iterative process which simulates natural selection. A population of strings, each representing a different autopilot controller, are maintained and evaluated for their quality of response each generation. The genetic operators, such as “reproduction”, “crossover”, “mutation”, and “fitness function” are then applied to evolve the population through a directed stochastic process.

Design Criteria

A set of classical design criteria was established including minimums on gain and phase stability margins, maximums on allowable cross-axis coupling for all axis permutations, maximum time-domain percent overshoot, and the basic requirement of positive stability requiring all closed loop poles be located in the open left-half-plane. Additionally, the desired controller should provide the highest bandwidth possible while maintaining those minimum requirements. The design criteria are thus broken into

two categories, primary and secondary, where the primary criteria represent hard constraints with specific values to be met or exceeded, and the secondary criteria represent open ended optimizations. The stability margin design specifications called for phase margins of at least 30 deg and gain margins of at least 4 dB. For added safety margin, an extra 10 deg of phase margin and 2 dB of gain margin were added to the design criteria.

Primary Criteria:

- All Poles in open LHP
- Phase Margins > 40 deg
- Gain Margins > 6 dB
- Peak Cross Coupling < -10 dB
- Peak Overshoot < 20%

Secondary Criteria:

- Maximize Closed Loop Bandwidths
- Maximize Sensitivity Bandwidths (As defined in Eq. 1)

Population Limits

The population was initialized with a uniform distribution of random numbers within limits that were pre-determined from root locus analysis. A locus of roots was generated for each autopilot gain and used to restrict its limits to realistic values that were not wildly unstable. Figure 17 shows two example loci used to determine population limits.

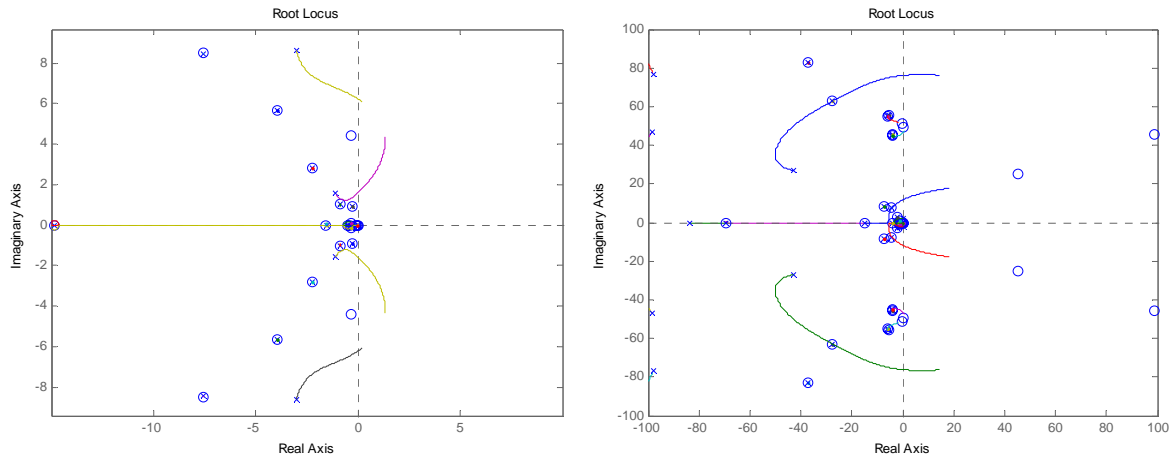


Figure 17. Root locus based population limiting.

Fitness Function

The genetic algorithm’s “Fitness Function” was designed as a weighted, multi-tiered sorting algorithm. Weighting factors were assigned to each of the primary design requirements, and cost values were computed for each controller string assigning a penalty for any design criteria not met. An important, yet subtle, detail of this cost assignment scheme was in offering no “extra credit” (or penalization) to those controllers that exceeded design requirements. A controller that just barely met primary design objectives was considered equally fit to a controller that far exceeded the requirements. The second tiered sort would then rank all controllers meeting primary design objectives by their overall speed of response. Two bandwidth metrics were used; the closed loop bandwidth and more conservative sensitivity bandwidth of each axis. Using this two-tiered approach, the evolution of gains was directed toward a controller with the fastest speed of response meeting all of the primary design objectives.

Gain Evolution

Figure 18 shows a representative convergence of the entire set of autopilot gains at various snapshots during the evolutionary process. It is always interesting to study the evolutionary behavior, to determine whether multiple optimal designs may possibly exist. This would manifest in the population of one or more gains migrating into two or more distinct “tribes” yielding close to equal performance characteristics. In such cases, further evaluation should be done studying the performance of each region selected by the genetic algorithm. In this case, however, the general trend is towards a single, global, optimum solution for the autopilot controller. The standard deviation associated with a given parameter is representative of the sensitivity of that parameter to the ultimate design goal. The last population set shown represents the 10th generation autopilot.

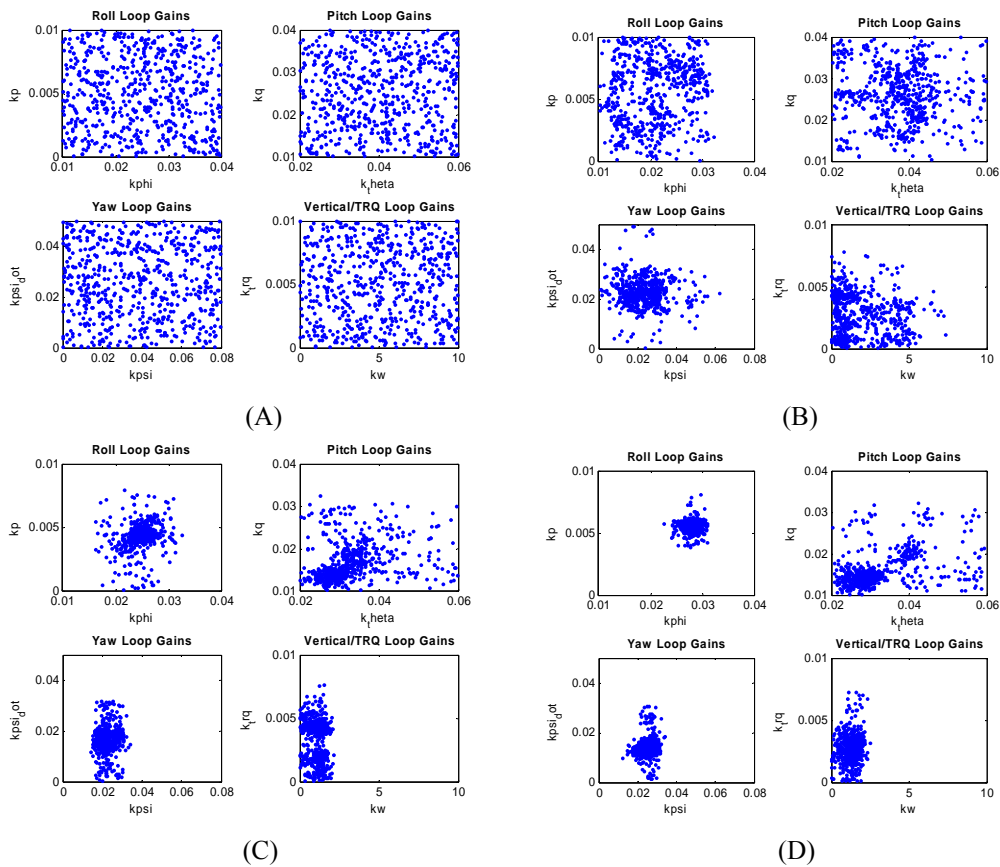


Figure 18. Gain evolution.

Autopilot Performance Results

The results of the genetic algorithm optimization can be seen in terms of time domain step responses for each

axis, and the frequency domain cross-axis attenuation. These results are shown by Figure 19.

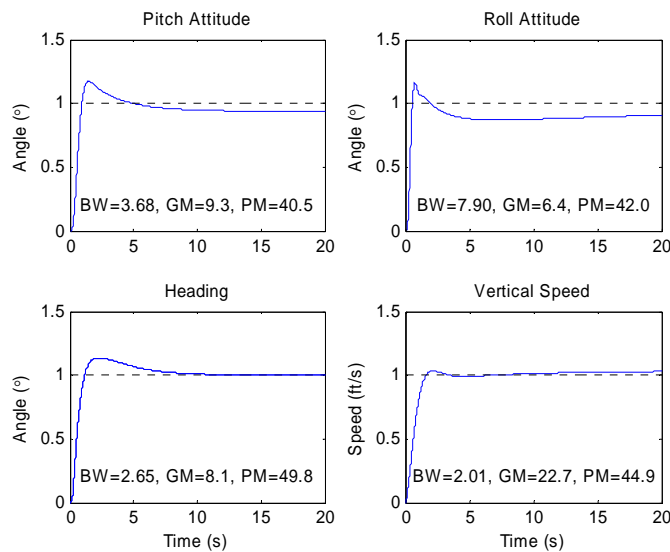


Figure 19a. Performance Results: Time Domain Response

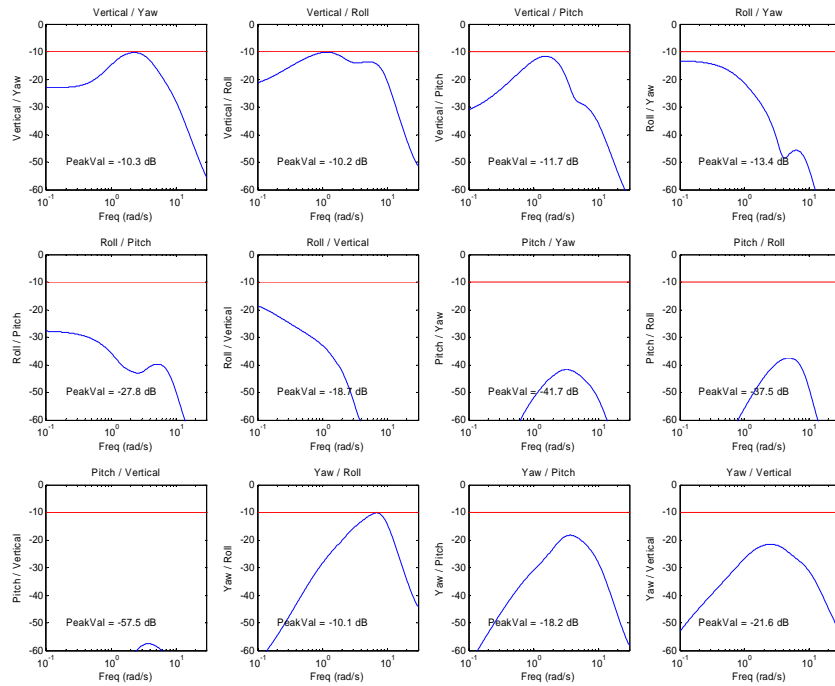


Figure 19b. Performance results: Frequency Domain Cross-Coupling

The performance metrics summarized in Table 5 show that the primary design criteria of gain margins, phase margins, and percent overshoot have all been met while maximizing the closed loop bandwidths.

Table 5. Autopilot performance results.

	Gain Margin (dB)	Phase Margin (deg)	Over Shoot (%)	Bandwidth (rad/s)
Pitch Attitude	9.3	40.5	17.5	3.68
Roll Attitude	6.4	42.0	15.5	7.90
Yaw Attitude	8.1	49.8	13.2	2.65
Vertical Speed	22.7	44.9	5.6	2.01

This table only partially captures the optimization that went on, however. Noticing, for example, that the vertical controller's gain and phase margin greatly exceed the design requirements, it would appear that the

vertical axis bandwidth could have been increased bringing these stability margins down to their minimums. This was not allowed by the genetic algorithm, however, as an additional primary design requirement on the maximum allowable cross-coupling between all axis permutations would have been violated for any additional speed increase on the vertical axis.

The cross-axis coupling for all axis permutations is summarized in Table 6. The design criteria was set at -10 dB maximum cross-coupling between all axes. The physical interpretation of this quantity is to ensure that any excitation of one axis does not couple into another axis by more than -10 dB, yielding a minimum of 68.4% attenuation. The vertical to yaw cross-coupling requirement, for example, thus ensures that a 1 ft/s vertical climb rate will induce no more than a 0.316 deg yaw motion as a result of this maneuver. Or a 500 ft/min vertical climb rate will induce no more than a 2.63 deg yaw motion, etc. There were three cross coupling responses (vertical to yaw, vertical to roll, yaw to roll) brought down to their minimums through this optimization process.

Table 6. Peak frequency domain cross-axis coupling.

Axis Permutation	Cross-Coupling (dB)
Vertical to Yaw	-10.3
Vertical to Roll	-10.2
Vertical to Pitch	-11.7
Roll to Yaw	-13.4
Roll to Pitch	-27.8
Roll to Vertical	-18.7
Pitch to Yaw	-41.7
Pitch to Roll	-37.5
Pitch to Vertical	-57.5
Yaw to Roll	-10.1
Yaw to Pitch	-18.2
Yaw to Vertical	-21.6

Comparison of Inner Loop Control Law Results

A comparison of the characteristics of the CONDUIT[®] and genetic control law syntheses will be shown in this section of the paper. The purpose of the comparison is to provide confidence the results are reasonable and to show that the performance of the MQ-8B is close to that which was successfully flown on the RQ-8A.

Table 7 compares the two MQ-8B inner loop designs against the RQ-8A.

Table 7. Comparison for RQ-8A and MQ-8B (CONDUIT[®] and genetic) designs.

	Pitch G.M. (dB)	Pitch P.M. (deg)	Roll G.M. (dB)	Roll P.M. (deg)	Yaw G.M. (dB)	Yaw P.M. (deg)	Collective G.M. (dB)	Collective P.M. (deg)
RQ-8A	9.72	41.83	6.26	26.2	12.9	79.75	19.9	86.9
Conduit	8.5	46.1	8.32	48.7	16.7	45	7.1	45
Genetic	9.3	40.5	6.4	42	8.1	49.8	22.7	44.9

	Pitch Crossover (rad/s)	Roll Crossover (rad/s)	Yaw Crossover (rad/s)	Collective Crossover (rad/s)	Pitch D.R.B. (rad/s)	Roll D.R.B. (rad/s)	Yaw D.R.B. (rad/s)	Collective D.R.B. (rad/s)
RQ-8A	3.24	3.98	3.45	1.44	1.1	1.77	1.05	1.4
Conduit	3.92	4.18	2.82	2.14	0.96	1.4	1.1942	0.98
Genetic	3.39	4.68	4.98	2.2	.949	1.75	1.21	1.209

G.M. = gain margin, P.M. = phase margin, D.R.B. = disturbance rejection bandwidth

In general, the table shows that both designs meet, or nearly meet the requirements for gain and phase margin from MIL-F-9490D (Ref. 8). The table also shows that the roll phase margin has been greatly improved from the RQ-8A for both the CONDUIT[®] and genetic methods of control gain optimization. The cross-over frequencies are very reasonable compared to the RQ-8A, and the disturbance rejection bandwidth was very similar to that of the RQ-8A. The only point of concern in the NGC design was the high cross over frequency in the yaw-axis, which was around the same frequency as the engine dynamics. However, this cross-over frequency is comparable to that of the RQ-8B, the design has reasonable stability margins, and moreover, the flight tests results (shown later) were similar to the good performance that was predicted in the simulation.

Overall, the two MQ-8B designs are consistent with each other, and also provide reasonable stability and performance as compared to the RQ-8A. This gave NGC confidence to finalize the inner loop (ACAH) gains. Once the inner loop gains were chosen, the design of the gains in the outer loop position and

velocity controllers was completed, as is discussed in the following section.

Outer Loop Design

As discussed previously, the outer loop functions control the vehicle's position with respect to a mission planned track, the altitude profile, the airspeed or groundspeed and the course, heading or sideslip angle depending on mission phase or the air vehicle operator's commands. The outer loop control laws use the same simple PID architecture as the inner loop with gains scheduled with true airspeed.

Designing the Gain Sets for the Outer Controllers

The outer loop gain synthesis used a less automated, more classical, loop-at-a-time approach to achieving similar stability and performance criteria as those of the Autopilot. The performance criteria contained in MIL-F_9490D (Ref. 8) was used as a rough guide, however to a certain extent there was some subjectivity involved in the assessment of outer loop response. Fundamentally the vehicle should fly appropriately (i.e. as a pilot might

fly) to maintain position, speed, altitude and heading, demonstrate adequate stability and resistance to environmental disturbances.

For each controller, root loci in the w' plane were used to place the most significant roots in a desirable position with respect to bandwidth, damping and stability. Linear step responses were then examined to verify adequate time domain characteristics. Stability margins were then generated by means of open loop Bode plots through all of the feedback and actuator paths. This analysis was repeated for each of the four "anchor" flight conditions to generate a schedule of gains.

The gain sets thus obtained were then exercised in the full-up non-linear simulation which takes into account rate and position limits, mode logic interactions as well as disturbances, noise on feedback signals etc.

Flight Test Results from the Unmanned MQ-8B Vehicle

The GNC software has the capability to inject doublets and frequency sweep test signals into the Autopilot output commands to the actuators. At this time, the MQ-8B has flown a total of 5 flights and only doublet maneuvers at hover have been completed. With these test maneuvers, we hope to demonstrate that, 1) the vehicle is safe to fly at the test flight condition, 2) good correlation between flight test and simulation exists at that flight condition, an indication of the quality of the aerodynamic derivative estimates.

The doublets were injected directly into the auto-pilot command path before the mixer. The doublets flown were of 4 second duration. Time history comparisons between flight test and simulation have been made for 1 degree amplitude doublets in hover. These comparisons are shown in Figures 23 through 26.

A flight test/simulation comparison is shown in Figures 23a and 23b for the 1 degree pitch axis doublet in hover.

In this axis the correlation between the flight test pitch rate response and that of the simulation was relatively poor with the simulation indicating a very well damped response and the actual flight data showing approximately 11% damping. As shown by Figure 6 earlier in this paper, the identified model matches the flight data accurately in the pitch axis, indicating that the identified model is likely not the reason for the mismatch, unless there are unknown differences between the manned version on which model identification was performed and the unmanned version of the MQ-8B. Roll and yaw rates show good correlation with the simulation, they are hardly excited, demonstrating minimal cross coupling between the pitch, roll and yaw axes.

Figures 24a and 24b show the flight test/simulation comparison for the 1 degree roll axis doublet. Excellent flight test/simulation correlation is demonstrated in the roll rate response. Pitch and yaw rates are hardly excited by the roll doublet.

Figures 25a and 25b show the flight test/simulation comparison for the 1 degree pedal doublet. Good correlation between flight test and the simulation is shown in the yaw rate response. Pitch and roll rates are hardly excited, in either simulation or flight test, demonstrating minimal cross coupling between the pitch, roll and yaw axes.

Figures 26a through 26d show the flight test/simulation comparison for the 1 degree vertical axis doublet. Minimal excitation is seen in the pitch, roll, and yaw rates. Good correlation between flight test and the simulation is shown in the velocity down response and normal acceleration responses. All other velocities and accelerations are unaffected.

With this limited data, except for the pitch response, there is good agreement between the simulation and flight test response. Work continues on determining the reasons behind the poor match in pitch response.

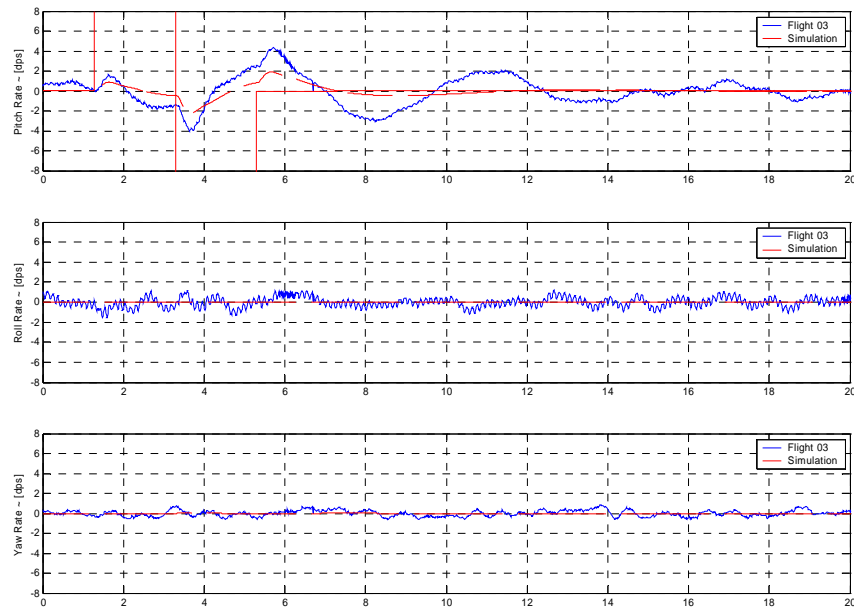


Figure 23a. Rates for 1 degree pitch axis doublet, hover flight phase.

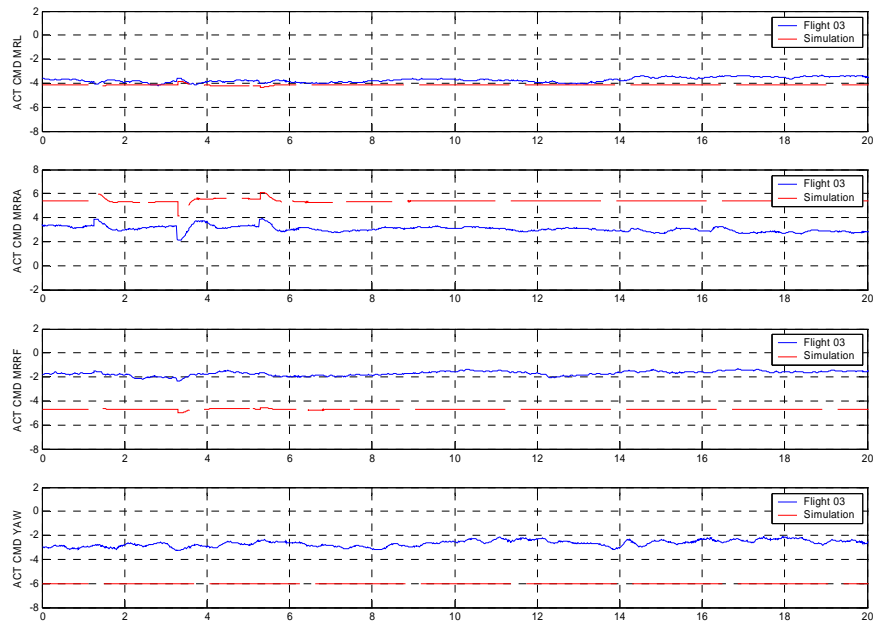


Figure 23b. Actuator commands for 1 degree pitch axis doublet, hover flight phase.

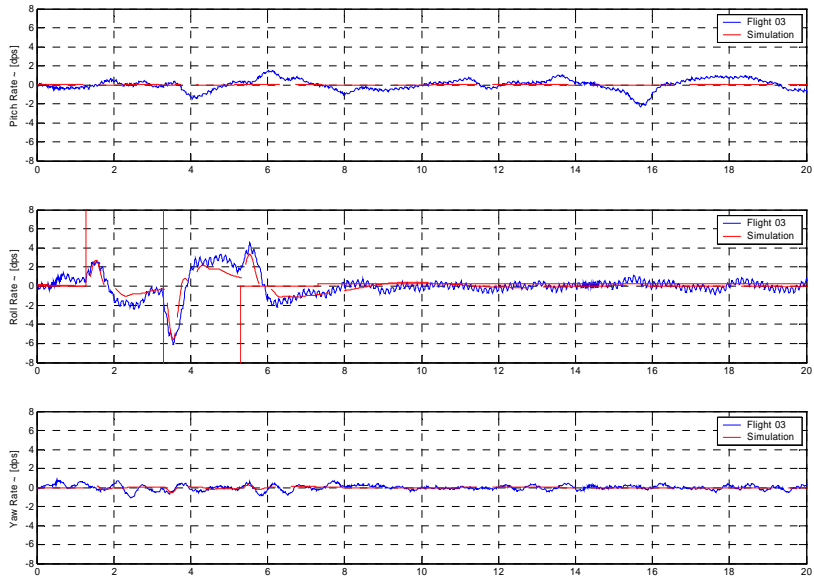


Figure 24a. Rates for 1 degree roll axis doublet, hover flight phase.

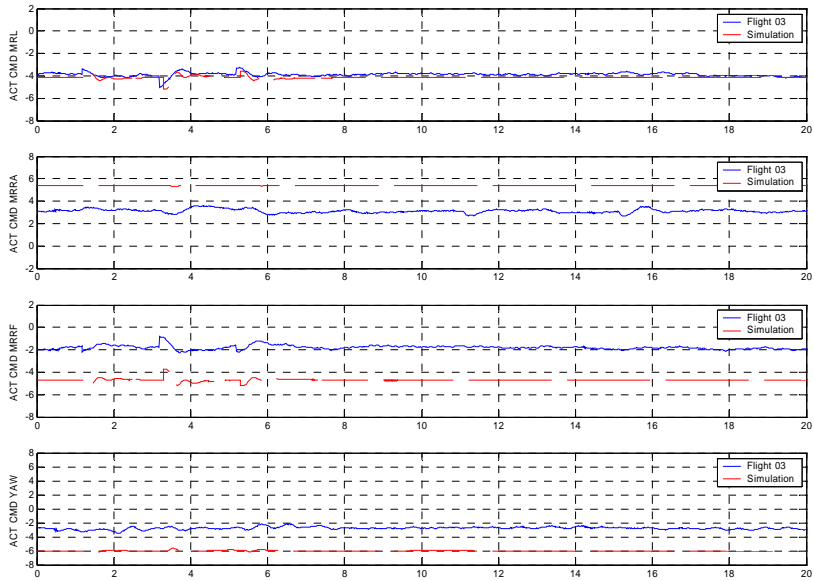


Figure 24b. Actuator commands for 1 degree roll axis doublet, hover flight phase.

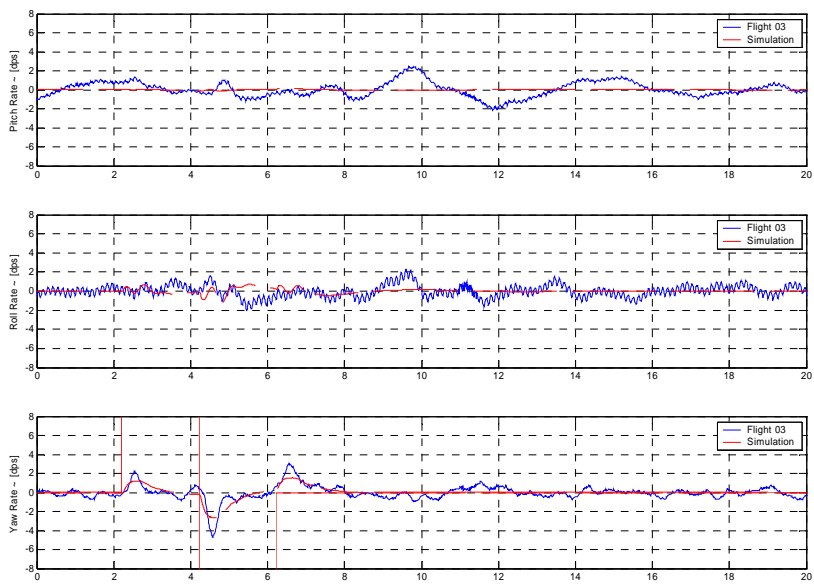


Figure 25a. Rates for 1 degree pedal doublet, hover flight phase.

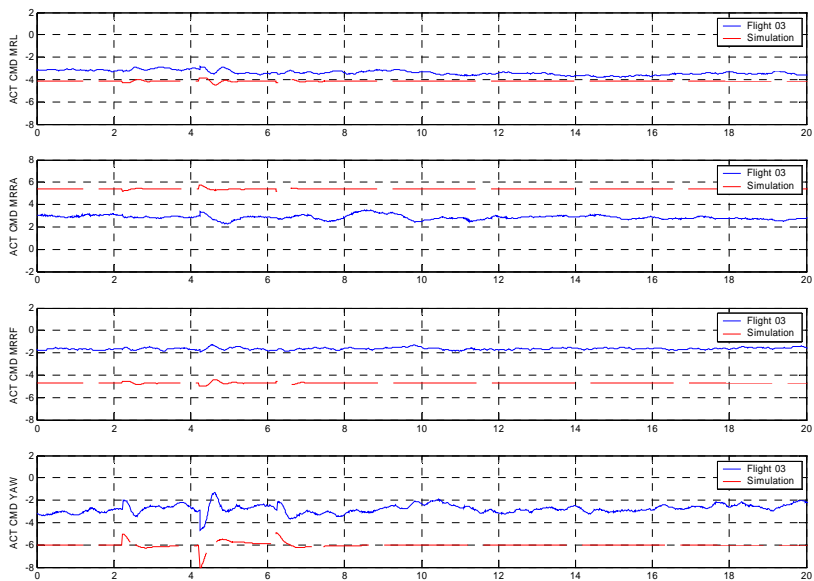


Figure 25b. Actuator commands for 1 degree pedal doublet, hover flight phase.

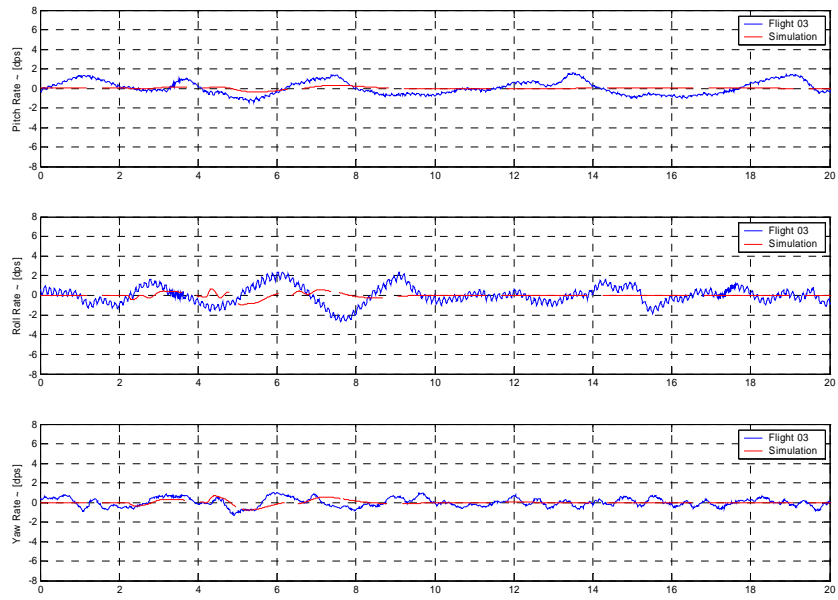


Figure 26a. Rates for 1 degree vertical axis doublet, hover flight phase.

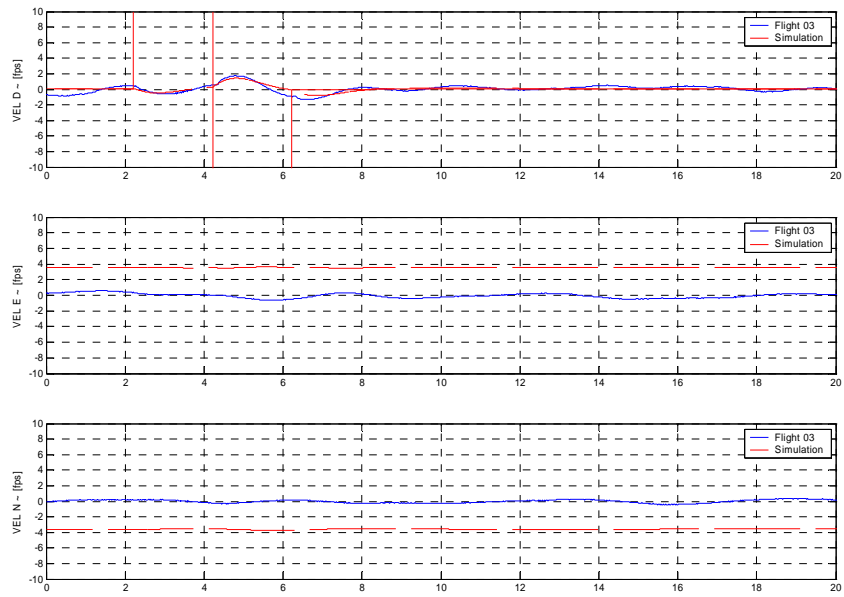


Figure 26b. Velocities for 1 degree vertical axis doublet, hover flight phase.

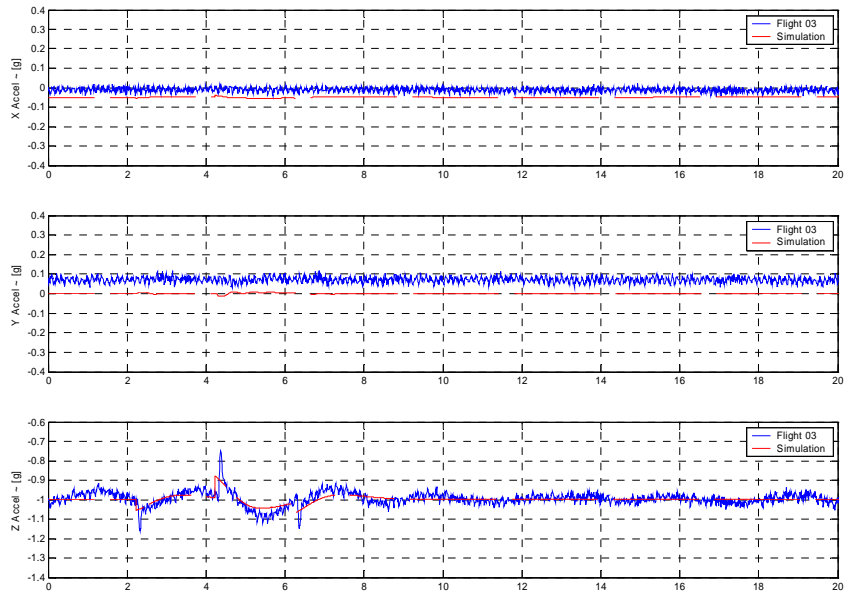


Figure 26c. Accelerations for 1 degree vertical axis doublet, hover flight phase.

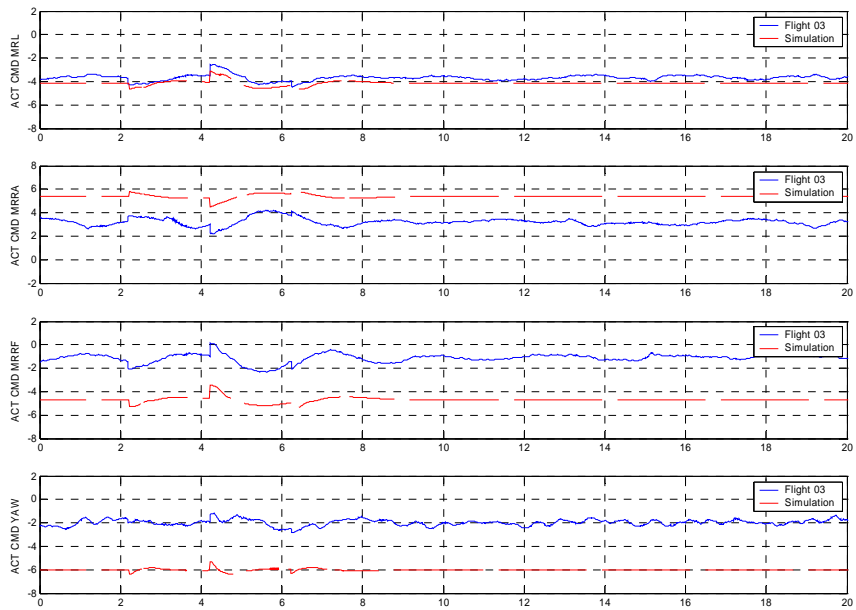


Figure 26d. Actuator commands for 1 degree vertical axis doublet, hover flight phase.

Conclusions

This paper documents the successful flight control system development for the MQ-8B from model identification to autopilot gain design to flight test. CIPHER[®] system identification methods were used to generate an accurate state-space model. NGC and the U.S. Army AFDD undertook parallel but distinct design paths for the Autopilot design at the hover flight condition. As of this writing, the MQ-8B has completed five successful test flights, involving several hovers. The following conclusions are drawn from this effort:

1. System identification provided efficient means for obtaining accurate models of the bare airframe dynamics, including engine response.
2. Two design methods were used to optimize the control laws for performance and stability requirements. These methods produced reasonably consistent results, lending confidence to the final design.
3. Flight tests to date have shown good closed-loop performance in hover.
4. In general, the full closed-loop simulation was accurate in predicting MQ-8B responses, although some discrepancies need to be investigated.

Acknowledgements

The authors wish to thank Erick Burger and Jann Mayer of the Northrop Grumman Fire Scout GNC team for their extensive contributions to this work.

References

1. Tischler, M. B. and Remple, R. K., *Aircraft and Rotorcraft System Identification: Engineering Methods With Flight Test Examples*, AIAA Aug 2006.
2. Colbourne, J. D., Tischler, M. B., and Rogers, K., "Flight Control Design for an Unmanned Rotorcraft Program with a Rapid Development Schedule," Proceedings of the American Helicopter Society 57th Annual Forum, Washington, DC, May 2001.
3. Tischler, M.B., Cauffman, M.A., "Frequency response method for Rotorcraft System Identification." *Journal of the American Helicopter Society*, Vol 37, No 3, Pgs 3-17, July 1992
4. Zivan, L., Tischler, M., B., "Development of Full Flight Envelope Helicopter Simulation Using System Identification," AHS 63rd Annual Forum and Technology Display, May 1 - 3, 2007, Virginia Beach, Virginia.
5. Harding, Jeff, Moody, Scott, "Identification of AH-64D Dynamics to Support Flight Control System Evaluations," Proceedings of the American Helicopter Society 61st Annual Forum, Grapevine, Texas, June 1-3 2005.
6. Tischler, M. B., et al, "A Multidisciplinary Flight Control Development Environment and Its Application to a Helicopter," *IEEE Control Systems Magazine*, Vol. 19, No. 4, pg. 22-33, August, 1999.
7. Anon, "Aeronautical Design Standard, Handling Qualities Requirements for Military Rotorcraft," US Army Aviation and Missile Command, USAAM-COM, ADS-33E-PRF, 21 March 2000.
8. "Military Specification, Flight Control Systems – General Specification for Design, Installation and Test of Piloted Aircraft," MIL-F-9490D (USAF), June 6, 1975
9. Harding, J.W., Moody, S.J., Jeram, G.J., Mansur, M.H., Tischler, M.B., "Development of Modern Control Laws for the AH64D in Hover/Low Speed Flight." American Helicopter Society 62nd Annual Forum, Phoenix, Arizona, May 9-11 2006.
10. Goldberg D., *Genetic Algorithms*, Addison Wesley, 1988.